ACS Sustainable Chemistry & Engineering

Research Article

Cite This: ACS Sustainable Chem. Eng. 2018, 6, 4829–4837

pubs.acs.org/journal/ascecg

Lab-Scale Alkaline Water Electrolyzer for Bridging Material Fundamentals with Realistic Operation

Wenbo Ju,[†] Meike V. F. Heinz,[†] Lorenzo Pusterla,[†] Matthias Hofer,[†] Benjamin Fumey,[‡] Roberto Castiglioni,[†] Marco Pagani,[†] Corsin Battaglia,[†] and Ulrich F. Vogt*[,†,§]

[†]Laboratory Materials for Energy Conversion, Swiss Federal Laboratories for Material Science and Technology (Empa), Überland Straße 129, 8600 Dübendorf, Switzerland

[‡]Urban Energy Systems Laboratory, Swiss Federal Laboratories for Material Science and Technology (Empa), Überland Straße 129, 8600 Dübendorf, Switzerland

[§]Faculty of Environment and Natural Resources, Crystallography, Albert-Ludwigs-University Freiburg, Tennenbacher Straße 4, 79106 Freiburg im Breisgau, Germany

ABSTRACT: Hydrogen produced by water electrolysis with renewable electricity is a reliable, affordable and environmental friendly energy carrier for future energy supply and storage. Alkaline water electrolysis is a well matured technique and proved to be suitable for large-scale applications. Materials development for alkaline water electrolyzers is still of interest for academia and industry to address the issues of low compatibility to renewable power sources. A lab-scale system for alkaline water electrolysis was developed, aiming to advance materials development and to bridge the intrinsic properties of materials with their performance under realistic operating conditions. As the smallest pressure-type electrolyzer, it is capable of working at 30 bar and 80 °C with continuous liquid electrolyte circulation. Experimental studies investigate the influence of temperature, pressure, and intrinsic properties of materials on voltage efficiency and hydrogen purity. With appropriate analysis, links between material specifications and overall performance can be established, encouraging new designs and material innovations for alkaline water electrolysis.

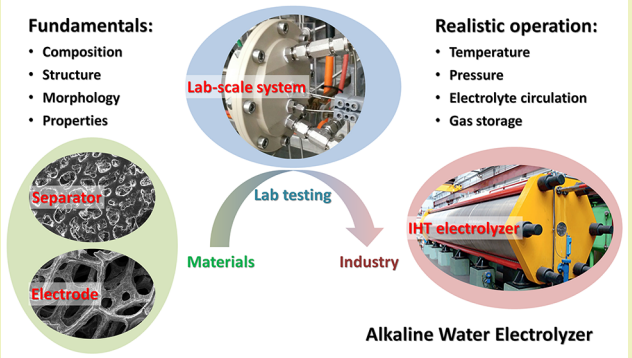

KEYWORDS: *Alkaline water electrolyzer, Pressure-type system, Voltage efficiency, Hydrogen purity*

INTRODUCTION

In 2016, global energy consumption reached the unprecedented amount of 13 910 million tonnes of oil equivalent (Mtoe) per year, which corresponds to an increase by 18% over the past 10 years or by a factor 1.5 over the past two decades.[1] Fossil fuels still dominate the global energy market despite of serious environmental and social threats such as air pollution, climate change, and exhaustion of natural resources. Establishing a sustainable energy economy is a critical and imperative challenge. Hydrogen as a clean energy carrier can address issues of sustainability, environmental emissions, and energy security. Applied either in its pure form or after conversion to synthetic fuels, hydrogen generated from renewables is an ideal transportation fuel aiming to reduce automotive emissions and dependence on fossil fuels.[2−4] Hydrogen can further be used as an energy storage medium to overcome the intermittency of renewable energy sources, thus balancing both daily and seasonal peak output and peak demand.[5−7]

The decomposition of water (H_2O) to hydrogen (H_2) and oxygen (O_2) has a large positive free energy change (ΔE), which, in the case of electrolysis, is supplied by electrical energy. The half and overall reactions in an alkaline solution can be written as

$$\text{Cathode: } 2H_2O + 2e^- \rightarrow H_2 + 2OH^- \quad (1)$$

$$\text{Anode: } 2OH^- \rightarrow \frac{1}{2}O_2 + H_2O + 2e^- \quad (2)$$

$$\text{Overall: } H_2O + \Delta E \rightarrow \frac{1}{2}O_2 + H_2 \quad (3)$$

The equilibrium cell voltage at standard condition (25 °C and 1 bar) is 1.23 V, which is derived from the reaction Gibbs free energy change of +237.1 kJ·mol^{-1}.[8] This is the minimum amount of electrical energy required for the reaction, while additional thermal energy should be supplied to keep a constant temperature. Under adiabatic condition, the enthalpy change (+285.8 kJ·mol^{-1})[8] is provided by electrical energy, leading to a thermoneutral voltage of 1.48 V. The equilibrium voltage depends strongly on temperature, that at 1 bar pressure the

Received: November 10, 2017
Revised: January 24, 2018
Published: February 15, 2018

DOI: 10.1021/acssuschemeng.7b04173
ACS Sustainable Chem. Eng. 2018, 6, 4829–4837

equilibrium voltage decreases from 1.23 V at 25 °C to 1.17 V at 100 °C for liquid water electrolysis, and from 1.17 V at 100 °C to 1.14 V at 200 °C for steam water electrolysis (shown in Figure 1 as solid lines). In contrast, the thermoneutral voltage

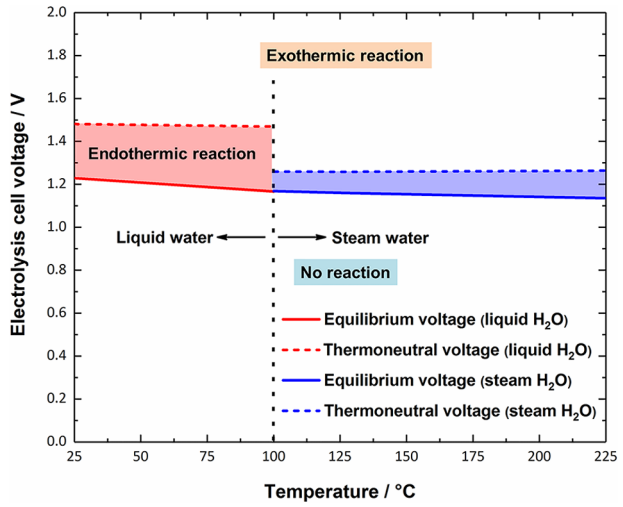

Figure 1. Equilibrium and thermoneutral voltages for water electrolysis as a function of temperature. Curves derived from the data in reference 8.

features weak dependence on temperature except for an abrupt drop from 1.48 to 1.26 V related to the phase change of water at 100 °C (shown in Figure 1 as dashed lines). As electricity has a significantly higher value than heat, lowering the equilibrium voltage is a strategy to save electric energy and thus improve cost effectiveness of alkaline electrolysis.

Liquid water electrolysis (or low-temperature water electrolysis) has been put into practice in three basic configurations: (1) proton exchange membrane (PEM) electrolysis using solid acidic polymer electrolyte,[9,10] (2) alkaline water (AW) electrolysis employing porous diaphragms infiltrated with alkaline solution,[11,12] and (3) anion exchange membrane (AEM) electrolysis applying solid anion polymer electrolyte.[13,14] PEM electrolyzers can operate at higher current densities (0.6−2.0 $A{\cdot}cm^{-2}$), and their advantages of good partial load toleration and rapid system response allows to work under a wide range of power input.[9,15] However, for large-scale application, further cost reduction and durability enhancement are needed.[9,16] AEM electrolysis is a developing technique with many unsolved issues, especially the chemical stability of AEMs.[17,18] AW electrolysis is a proven and cost-effective technique, which has been commercialized at large scale. Ursua et al.[19] summarized the main AW electrolysis systems, which have rated power in the range of 1.8 kW−3.6 MW, hydrogen production rates from 0.265 to 760 N $m^3{\cdot}h^{-1}$, and voltage efficiencies in the range of 47%−82%. The energy efficiency of AW electrolyzers with zero-gap cell configuration is comparable to PEM electrolyzers.[20] Moreover, the relatively low investment cost and long lifetime (up to 90 000 h for stacks and up to 30 y for systems) keep AW electrolyzers at the leading position in the water electrolysis market.[9,20,21]

However, the competitiveness of AW electrolyzers is limited by several disadvantages, such as relatively low current densities (0.2−0.4 $A{\cdot}cm^{-2}$) and low partial load toleration.[19,20] Diaphragms, which feature microporous structure for liquid

Scheme 1. Schematic Structure of the Lab-Scale AW Electrolysis System[a]

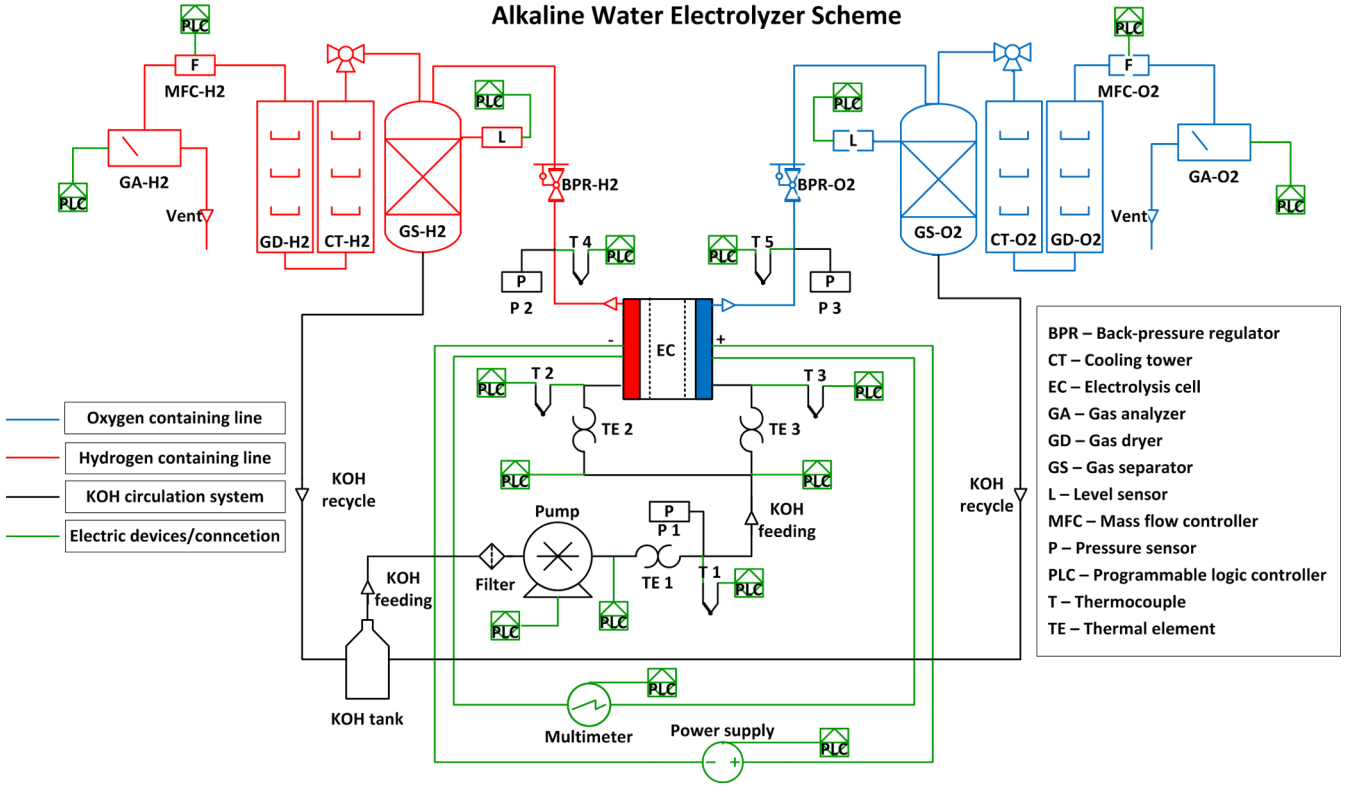

[a]Subsystems for hydrogen, oxygen, liquid electrolyte, and power/control system are highlighted in red, blue, black, and green, respectively.

DOI: 10.1021/acssuschemeng.7b04173
ACS Sustainable Chem. Eng. 2018, 6, 4829−4837

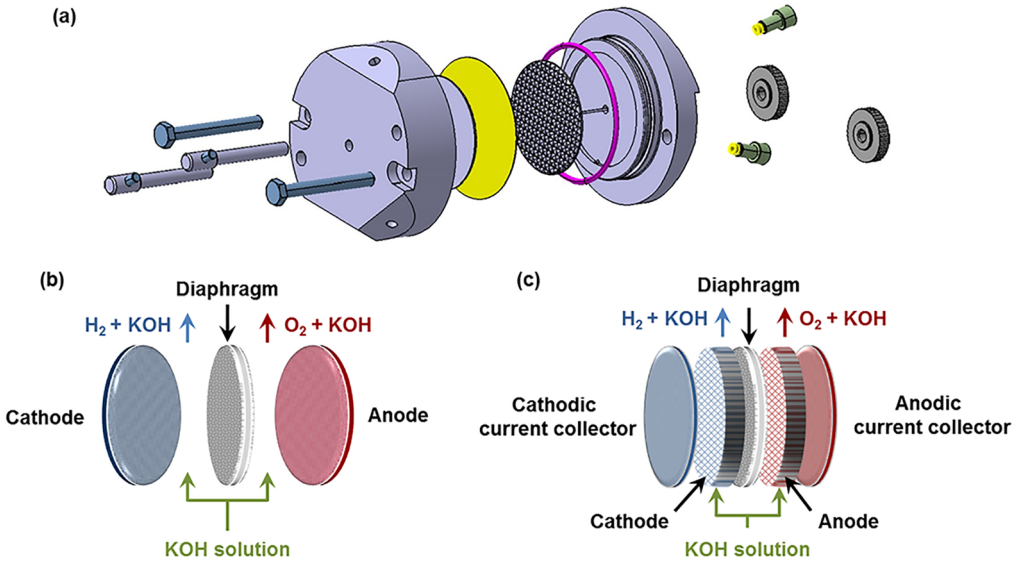

Figure 2. Schematic structures of electrolysis cell (a), gap electrode assembly (b), and zero-gap electrode assembly (c).

electrolyte infiltration, enable gas crossover especially at high system pressure, leading to impurities and even safety hazard.[20,22] Either thickening the diaphragm or reducing pore sizes can lower gas crossover, but the ohmic loss in electrolyte increases, consequently lowering energy efficiency. Energy losses associated with activation of electrode reactions and deactivation of catalyst layers after long-time operation are still challenges that need to be addressed by the development of more active and robust electrocatalysts.

A lab-scale AW electrolysis system has been developed in our laboratory to advance the lab-scale material research, and to bridge the intrinsic properties of materials with their performance under realistic operating conditions. The system is able to work at a pressure up to 30 bar and a temperature up to 80 °C with electrolyte circulation rate up to 200 mL·min^{-1}. Applied current, voltage and gas purity can be recorded in real time. Technical details of the lab-scale AW electrolysis system are discussed, and experimental studies with model electrodes and diaphragms reveal the influence of temperature, pressure, and current density on cell voltage and gas purity.

EXPERIMENTAL SECTION

System Description. The lab-scale AW electrolysis system is shown schematically in Scheme 1. It consists of five functional subsystems: (1) electrolysis cell, (2) hydrogen separation and analysis, (3) oxygen separation and analysis, (4) liquid electrolyte circulation, and (5) power supply, control, and data acquisition system. The construction materials of pipes, tanks, gaskets, etc., are stainless steel because of their compatibility with temperature up to 80 °C.[23] Liquids and gases are transported in stainless steel Swagelok pipes and corresponding fittings. The diameters range from 3 to 10 mm depending on location. Three-way valves are used to switch between different settings of the system including normal operation, shutdown, system filling, flushing, and calibration.

The electrolysis cell is a single cell with monopolar configuration. Polyether ether ketone (PEEK) is used for the cell structure, since it matches the specifications of chemical durability against alkaline, excellent mechanical resistance to high temperature and pressure, and electric insulation. Figure 2a shows the three-dimensional structure of the cell. Both the gap electrode assembly (Figure 2b) and the zero-gap electrode assembly (Figure 2c) are available. The diaphragm thickness is variable from 0.5 mm up to 2.5 mm. Disc-shape electrodes have a diameter of 50 mm and a maximum thickness of 2 mm. Liquid electrolyte is fed into the cell through the inlet at the bottom, and gas−liquid mixture leaves the compartment from the outlet at the top.

During electrolysis, the gas−liquid mixture from the electrolysis cell flows into the separator. Gas products leave from the upper exit, and flow through a cooling tower and a silica-gel dryer. Meanwhile, liquid electrolyte flows through the bottom exit, and recycles into the solution tank. Hydrogen and oxygen have two independent gas separation and analysis subsystems. Since mass flow controllers (Bronkhorst, F-201CI) and gas analyzers (LFE-CONTHOS 2) do not have tolerance to corrosive liquids, the overflow of alkaline solution should be prevented. A potentiometric level sensor (Baumer, LSP 05X) is used in each separator to measure the liquid level. If the liquid level in either separator is higher than 70%, the power supply for electrolysis will shut down. Mass flow controllers are used to control the system pressure and to balance the liquid level in both separators. The maximum flow rates for hydrogen and oxygen are 500 and 250 mL·min^{-1}, respectively. The gas purity is analyzed online by the thermal conductivity detector (TCD) with a quick response time of 2 s.[24] In this system, gas analyzers are calibrated for measuring gas purities in the range of 98−100%.

The electrolyte circulation is driven by a micro annular gear pump (HNP Mikrosysteme, mzr-7205) with flow rates in the range of 0.048−288 mL·min^{-1}.[25] A filter is placed before the inlet of the pump to capture dregs. Three heating devices are used to heat the electrolyte. One is a heating module integrated around the pump head, which is capable of providing up to 150 W output. The other two modules are rope heaters (Omegalux, FGR) wound around the tubes connecting to the cell inlets. They are able to provide up to 400 W output, and assist the heating module to heat electrolyte up to a set point from 45 to 80 °C. Temperatures at the pump outlet as well as in the two compartments of the electrolysis cell are monitored by thermocouples.

The energy for electrolysis is provided by a DC power supply (AIM-TTI, TSX3510P) with an output current range of 0−10 A. Communication is carried out by a serial port. The current is set by the user or program for stepwise change or to a constant value, while the voltage is adjusted by an internal voltage control loop. The resolutions of current output and voltmeter are 10 mA and 10 mV, respectively.[26]

In order to control and monitor the electrolysis system, a software package was developed within the LabVIEW environment, which guarantees maximum flexibility. Various sensors and control units can be straightforwardly integrated, and further extensions are allowed. The software provides two operation modes: one is the manual mode, in which users can manually adjust set points for pressure, temperature, current density and electrolyte circulation speed; the other one is the automatic mode, in which the system operates according to predefined profiles of the aforementioned parameters.

DOI: 10.1021/acssuschemeng.7b04173
ACS Sustainable Chem. Eng. 2018, 6, 4829−4837

The automatic mode allows operation with variable current profiles to simulate the case of electricity from renewable sources. The current−voltage characteristic, gas purities, and cell temperature fluctuation are recorded and graphically visualized in real time. The software also incorporates several security functionalities, e.g., overheating protection, overflow protection, and emergency cutoff.

Materials for Demonstration. Nickel plates (BGH, 99.5%) with a diameter of 50 mm and a thickness of 2 mm are used as both anode and cathode. Both electrode surfaces are unactivated nickel. The front surfaces of both nickel plates are cut with laser beam for trapezoidal prism arrays. For each trapezoidal prism, the base length, top length and height are 3 mm, 1 mm, and 1 mm, respectively. The top surface of the trapezoidal prism is pressed against the diaphragm, while notches among trapezoidal prisms offer space for liquid and gas transport. The well-defined surface structure ensures a reproducible contact pressure between electrodes and diaphragm. The geometric area of each nickel plate, which is 19.63 cm^2, equals the cell area, and the current density discussed in this work is normalized to the cell area. Each nickel plate is spot-welded to two nickel wires (BGH, 99.5%) at the back side. One connects to the power output for electrolysis, and the other one is used to measure the cell voltage.

Commercially available Zirfon diaphragms (Agfa, Perl utp 500) are used as gas separators. The thickness of the diaphragm is 0.5 mm. Each diaphragm is cut to a round shape with a diameter of 85 mm, which is much larger than the diameter of cell (50 mm). The broad edge of the diaphragm is tightly pressed by the walls of the two cell compartments to avoid gas leakage. Thirty wt % KOH solution, prepared by dissolving KOH pellets (Sigma-Aldrich, 85.0%) in deionized water, is used as electrolyte. The conductivity of freshly prepared 30 wt % KOH solution is 625 $mS \cdot cm^{-1}$ at 25 °C.

RESULTS AND DISCUSSION

Characterization of Cold Start. A cold-start procedure is applied to warm the electrolysis system up to normal operating conditions. In the automatic mode, set points for cell temperature, system pressure, and electrolyte circulation speed are predefined.

The temperature of the electrolyte at the inlet of the cathodic compartment is used to represent the cell temperature. Figure 3(a) shows the increase of cell temperature from ambient (24 °C) to the set points of 30 °C (blue circles) and 80 °C (red diamonds). When the temperature set point is lower than 45 °C, the electrolyte is heated individually by the heating module integrated around the head of the circulation pump. The cell temperature increases from ambient up to 30 °C in 3.5 min, and overshoots to 31 °C due to the high power output for fast heating. After around 10 min, the cell temperature is stabilized in the range of 30 ± 0.5 °C. For temperature set points higher than 45 °C, the system is heated additionally by the two rope heaters. For the set point of 80 °C, it takes around 3 min to preheat all heating devices. When all the three devices reach the suggested operating temperatures, they heat the electrolyte up to 79 °C in 33 min. With the increase of cell temperature, the heating efficiency becomes lower due to enhanced heat losses through conduction and radiation. When the cell temperature is higher than 79 °C, the heating module is adjusted by a feed forward controller for a slow approach to 80 °C. The heating for 80 °C takes 42 min. The system is designed for operating at temperatures from ambient to 80 °C, and any temperature set point in this range can be reached within 42 min.

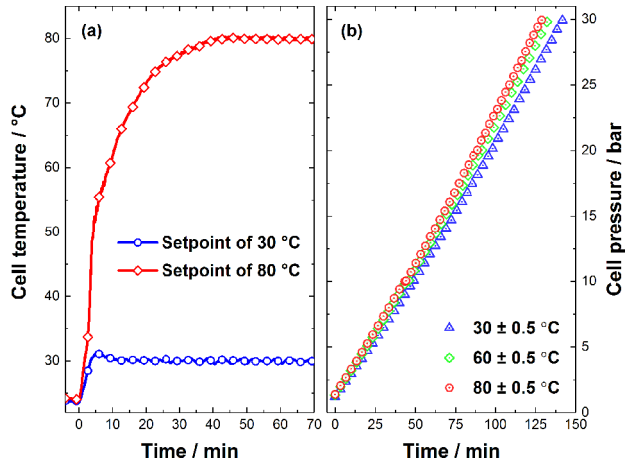

Figure 3. (a) Cell temperature during heating processes to set points of 30 and 80 °C. (b) Cell pressure during pressurization from 1 to 30 bar at 30, 60, and 80 °C, respectively.

The system is pressurized solely by electrolytically produced gases. In the pressurization mode, oxygen is stored in the oxygen subsystem. Meanwhile, half of the hydrogen is stored in the hydrogen subsystem. The mass flow controller in the hydrogen subsystem adjusts the flow rate, and balances the pressures in the two compartments. A current density of 502 $mA \cdot cm^{-2}$ is used for pressurization. Figure 3b shows the pressure-time curves at temperatures of 30, 60, and 80 °C, respectively. At 80 °C, the system pressurizes from 1 to 30 bar in 129 min, while the time for the same pressure set point is 134 min at 60 °C and 140 min at 30 °C. Assuming an ideal faradaic efficiency for water electrolysis (100% charge transfer for water decomposition),[27] the production rate of oxygen, r_{O_2}, is proportional to the current density, j_c, which can be expressed as

$$r_{O_2} = \frac{dN_{O_2}}{dt} = \frac{1}{nF} \cdot \frac{dQ}{dt} = \frac{A}{nF} \cdot j_c \quad (4)$$

where A is the cell area, Q is transferred charge, n is stoichiometric number of electrons involved in the oxygen evolution reaction (4 electrons for 1 O_2 molecule), and N_{O_2} is molar amount of produced oxygen. F is the Faraday constant. The initial gas volume of the oxygen subsystem approximates 20 mL for all measurements. It is assumed that the gas volume, V, keeps a constant for short-time electrolysis. At a fixed temperature, T, the pressurization rate, p_{O_2}, can be expressed as

$$p_{O_2} = \frac{dP_{O_2}}{dt} = \frac{RT}{V} \cdot \frac{dN_{O_2}}{dt} = \frac{ART}{nFV} \cdot j_c \quad (5)$$

where P_{O_2} is the pressure in the oxygen subsystem, and R is the universal gas constant. When oxygen is produced with a constant current density, the pressurization rate is proportional to temperature. The pressurization at high temperature is more efficient.

Hydrogen Purity. The hydrogen production capacity of this lab-scale AW electrolyzer is the smallest in all reported AW electrolysis systems. At the maximum current density of 502 $mA \cdot cm^{-2}$, taking into account the cell area of 19.63 cm^2 and assuming an ideal faradaic efficiency, the hydrogen production rate is 0.184 $mol \cdot h^{-1}$, or 4.50 $l \cdot h^{-1}$ at 25 °C. The system is very sensitive to gas impurities due to the small capacity, so that it is capable of comparing the performance of separators with small differences.

Table 1 lists hydrogen purities measured at fixed temperatures and pressures at a current density of 502 $mA \cdot cm^{-2}$. The highest hydrogen purity, which is recorded at 1 bar and 30 °C,

DOI: 10.1021/acssuschemeng.7b04173
ACS Sustainable Chem. Eng. 2018, 6, 4829−4837

Table 1. Hydrogen Purities at Selected Temperatures and Pressures[a]

Pressure (bar)	Hydrogen purity (%)			
	30 °C	40 °C	60 °C	80 °C
1	99.88 ± 0.03	99.69 ± 0.10	99.63 ± 0.12	99.60 ± 0.13
10	99.31 ± 0.03	98.96 ± 0.19	98.87 ± 0.25	98.85 ± 0.27
20	98.60 ± 0.11	98.13 ± 0.12	98.06 ± 0.06	98.04 ± 0.04

[a]A constant current density of 502 mA·cm^{-2} was applied for water electrolysis.

is 99.88 ± 0.03%. This value is comparable to reported hydrogen purities obtained from AW electrolyzers working at ambient pressure with Zirfon diaphragms for gases separation.[28,29] The cell temperature influences the hydrogen purity slightly. At 1, 10, and 20 bar, the hydrogen purity decreases by around 0.29%, 0.46%, and 0.56%, respectively, with the increase of cell temperature from 30 up to 80 °C. The slight decrease of hydrogen purity indicates more oxygen permeating into the hydrogen subsystem. It is attributed to the increase of oxygen diffusion coefficient at high temperature, although the oxygen solubility becomes lower with the increase of temperature.[30,31] Cell pressure influences the hydrogen purity significantly. From 1 to 20 bar, the hydrogen purity decreases by 1.28% at 30 °C and more than 1.50% at other three investigated temperatures. The pressure dependency of hydrogen purity can be attributed to the pressure-dependent oxygen permeation rate into the hydrogen subsystem. Oxygen diffusion and oxygen permeation caused by electrolyte cross-permeation are considered to be the two major pathways for oxygen permeation. According to the study of hydrogen permeation through Zirfon diaphragms by Schalenbach et al.,[32] the oxygen permeation rate, $\overline{r}_{O_2}$, can be expressed similarly as

$$\overline{r}_{O_2} = \frac{d\overline{N}_{O_2}}{dt} = -(\Phi_{O_2}^{Fick} + \Phi_{O_2}^{Darcy})\cdot A = \left(D_{O_2}S_{O_2} + \frac{K}{\eta}S_{O_2}\Delta P\right)\cdot\frac{A}{d}\cdot P_{O_2} \quad (6)$$

where $\overline{N}_{O_2}$ is molar amount of permeated oxygen, $\Phi_{O_2}^{Fick}$ is the oxygen diffusion flux, and $\Phi_{O_2}^{Darcy}$ is the oxygen permeation flux caused by electrolyte permeation driven by a differential pressure ΔP. D_{O_2} and S_{O_2} are the diffusion coefficient of oxygen in the diaphragm and the solubility of oxygen in the used KOH solution, respectively. d is the thickness of the electrolyte, which equals the thickness of the diaphragm. K and η are the permeability of electrolyte in the diaphragm and the viscosity of electrolyte, respectively. P_{O_2} is the partial pressure of oxygen in the oxygen subsystem, which approaches to the cell pressure, P, due to the relative high oxygen purity (≥96%). In eq 6, the reverse transport of oxygen from the hydrogen subsystem to the oxygen subsystem is neglected due to the low concentration of oxygen in hydrogen (≤2%). At a certain temperature, K, η, D_{O_2} and S_{O_2} have constant values. The differential pressure ΔP between the two compartments is dynamically adjusted by mass flow controllers, so that its average value is assumed to be constant as well. Therefore, the oxygen permeation rate is linearly correlated to the cell pressure, which agrees very well to experimental results listed in Table 1.

Hydrogen purity is investigated at a low current density and in a shut-down/restart process. Figure 4 shows the profile of applied current densities (blue solid line) and hydrogen purities at 30 (red dotted line) and 80 °C (red dash-dotted line). Before

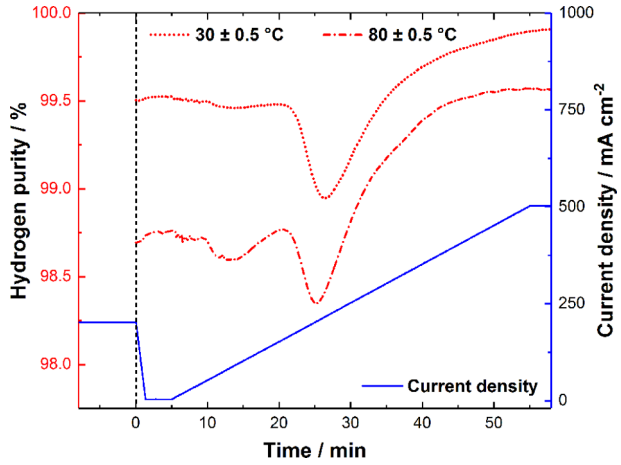

Figure 4. Profiles of applied current density and resulting hydrogen purities in shut-down/restart experiments at cell temperatures of 30 ± 0.5 °C and 80 ± 0.5 °C.

shutting down the power supply, the electrolyzer is working at a low current density mode that the current density is 202 mA·cm^{-2}. The hydrogen purities at this current density are 99.49 ± 0.03% at 30 °C and 98.68 ± 0.08% at 80 °C. When the system is switched to the standby mode (at 0 min), the current density decreases stepwise to 0 mA·cm^{-2} in 1.3 min, and it is kept for another 3.7 min. After 5 min at the standby mode, the current density increases from 0 up to 502 mA·cm^{-2} with a stepwise change of 1 mA·cm^{-2} per 5 s. Afterward, the current density is held at 502 mA·cm^{-2} for 4 min. The significant drop of hydrogen purity is observed after 20 min of switching off the power supply, which is due to the time delay caused by the transport of gases to the gas analyzer. The 5 min standby mode leads to almost 5 min continuous drop of hydrogen purity, and the lowest hydrogen purities are 98.95% at 30 °C and 98.35% at 80 °C, indicating a strong influence of intermittent power supply to the gas purity. When power is restored, both hydrogen purities start to increase. At 502 mA·cm^{-2}, the recorded highest hydrogen purities are 99.91% at 30 °C and 99.57% at 80 °C, and both values are higher than those recorded at the current density of 202 mA·cm^{-2}.

According to the study of hydrogen purity at different temperatures, pressures and current densities, the AW electrolyzers based on state-of-the-art materials (Ni based electrodes and Zirfon diaphragms) are recommended to work at a low pressure and a high current density for high-purity hydrogen. It is still a challenge to couple AW electrolysis systems with renewable sources, since gas purities drop significantly, even lower than accepted thresholds for operation, at low current or a standby mode. The high cell temperature may cause a slight decrease of hydrogen purity, but, comparing to the improvement in energy efficiency by temperature increase, the drawback of low hydrogen purity can be neglected.

DOI: 10.1021/acssuschemeng.7b04173
ACS Sustainable Chem. Eng. 2018, 6, 4829−4837

Reaction Kinetics. The voltammetric curves for water electrolysis were recorded at 30, 60, and 80 °C (shown in Figure 5a). The cell pressure for all measurements was set to 30 bar. The current density was increased stepwise by 1 mA·cm^{-2} per 5 s. An obvious shift of the voltammetric curve to lower cell voltage at high temperature indicates the improvement of reaction kinetics. The overpotential at 50 mA·cm^{-2}, η_{50}, which is the difference between the cell voltage at 50 mA·cm^{-2} and the corresponding equilibrium voltage, decreases by 0.132 V along with the temperature increase from 30 to 80 °C.

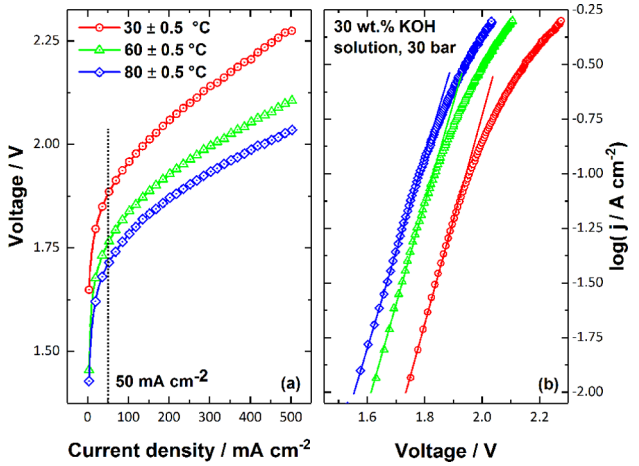

Figure 5. Voltammetric curves (a) and their Tafel plots (b) for water electrolysis at 30 ± 0.5, 60 ± 0.5, and 80 ± 0.5 °C. The cell pressure for all measurements is 30 bar. The current density, j, increases stepwise by 1 mA·cm^{-1} per 5 s from 0 to 502 mA·cm^{-1}.

The exponential behavior of these curves at low current densities is analyzed in Tafel plots (shown in Figure 5b). The Tafel slope is obtained by fitting the linear part of the Tafel curve, and the exchange current density is obtained by extrapolating the linear fitting to the equilibrium voltage. Tafel slopes, b, and exchange current densities, j_0, at the three temperatures are summarized in Table 2. The exchange current density increases from 0.022 mA·cm^{-2} at 30 °C to 0.190 mA·cm^{-2} at 80 °C, which confirms the increase in reaction kinetics with temperature.

In this two-electrode system, the overpotential, η, at low current densities comes primarily from the activation of both the hydrogen and the oxygen evolution reaction (HER and OER):

$$\eta = \eta_{HER} + \eta_{OER} \tag{7}$$

Although the contribution of each reaction to the overpotential cannot be distinguished, the current density, j, of the full cell is still a function of the overpotential η, which can be expressed as[23]

$$j = j_0 \cdot 10^{\eta/b} \tag{8}$$

The Tafel slope b is the superposition of the Tafel slopes for both the HER (b_{HER}) and the OER (b_{OER}):

$$b = b_{HER} + b_{OER} \tag{9}$$

For the HER, a nickel hydride (NiH_x) surface should be taken into account, due to the simultaneous formation of NiH_x during HER.[33,34] The reaction rate of the HER on a NiH_x electrode is limited by the combination of a hydrogen atom in water with an adsorbed hydrogen atom on the electrode surface (Heyrovsky step), and the Tafel slopes, b_{HER}, can be theoretically calculated with $4.6RT/F$.[35] At 30, 60, and 80 °C, the theoretical values are 120, 132, and 140 mV·dec^{-1}, respectively, which are listed in Table 2 as b_{HER}. For the OER, the rate-determining step on an oxidized nickel surface in alkaline solutions is the formation of an oxyhydroxide (−OOH) species by bonding a hydroxide ion (OH^-) on an adsorbed oxygen atom (−O).[36,37] A Tafel slope of $4.6RT/3F$ is suggested for this intermediate reaction at low current densities.[36] However, many authors observed much higher values of Tafel slopes in concentrated alkaline solutions.[38−41] Kibria et al.[38] reported that the Tafel slopes for the OER on a Ni electrode in 30 wt % KOH solution changed from 82 mV·dec^{-1} at 30 °C to 78 mV·dec^{-1} at 70 °C. Choquette et al.[39] observed an almost constant value of 80 mV·dec^{-1} on Raney-Ni electrode in 32 wt % KOH solution at temperatures from 54 to 69 °C. Nadesan et al.[40] reported the Tafel slope of 85 mV·dec^{-1} for the OER on nickel oxide electrodes at current densities between 5 and 100 mV·cm^{-2}. In order to analyze the OER in this work, Tafel slopes obtained experimentally in concentrated KOH solutions, are used as references. Since the reported Tafel slopes are not very sensitive to temperature change (80 ± 2 mV·dec^{-1} at temperatures from 30 to 70 °C),[38,39] the Tafel slopes for the OER (b_{OER}) are assumed to be 80 mV·dec^{-1} for all the three temperatures in this work. The sum of b_{HER} and b_{OER} at each temperature is listed in Table 2 as $b_{HER} + b_{OER}$. The value agrees very well with the measured Tafel slope b at each temperature, and the increase of Tafel slope b with temperature can be attributed to the increase of the Tafel slope for the HER (b_{HER}).

Potential Drop in Electrolyte. The temperature-dependent cell voltages were measured at a current density of 502 mA·cm^{-2} from 30 to 80 °C at 30 bar. All measured cell voltages are shown in Figure 6a as black diamonds. The cell voltage is 2.281 V at 30 °C, and it decreases by 0.275 V, down to 2.006 V at 80 °C. The voltage efficiency of the cell, measured relative to the

Table 2. Tafel Parameters and Overpotentials at 50 mA·cm^{-2} for the Full Cell Reactions at 30 ± 0.5, 60 ± 0.5, and 80 ± 0.5 °C; Tafel Slopes for the HER and the OER are Obtained by Referring Literature

T (°C)	U_{eq}[a] (V)	η_{50}[b] (V)	j_0 (mA·cm^{-2})	b (mV·dec^{-1})	b_{HER}[c] (mV·dec^{-1})	b_{OER}[d]/ (mV·dec^{-1})	$b_{HER} + b_{OER}$ (mV·dec^{-1})
30 ± 0.5	1.253	0.627	0.022	194	120	80	200
60 ± 0.5	1.231	0.528	0.106	210	132	80	212
80 ± 0.5	1.216	0.495	0.190	218	140	80	220

[a]The equilibrium voltages, U_{eq}, at 30 bar and different temperatures are calculated based on empirical equations in reference 42. [b]The overpotential at 50 mA·cm^{-2} is the difference between the cell voltage at 50 mA·cm^{-2} and the corresponding equilibrium voltage at the same temperature. [c]Tafel slopes for the HER, b_{HER}, are calculated based on $4.6RT/F$. [d]Tafel slopes for the OER, b_{OER}, are assumed to be a constant value of 80 mV·dec^{-1} according to experimental results in literature.[38−40]

DOI: 10.1021/acssuschemeng.7b04173
ACS Sustainable Chem. Eng. 2018, 6, 4829−4837

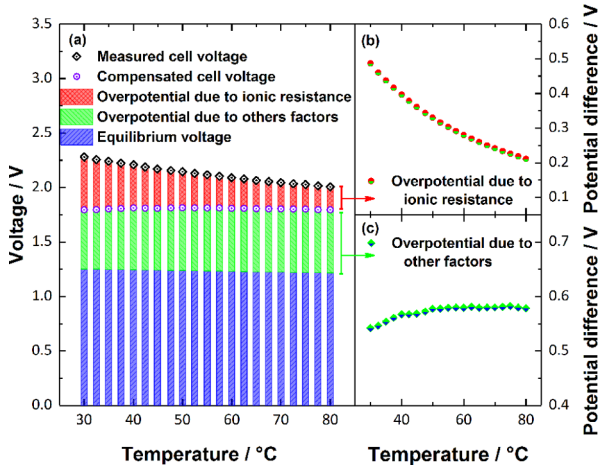

Figure 6. (a) Measured cell voltages and the share of equilibrium voltages, potential drop in electrolyte, and overpotentials due to other factors as a function of temperature. (b) Overpotentials due to ionic resistance. (c) Overpotentials due to other factors except ionic resistance.

equilibrium voltage of 1.253 V at 30 °C and 1.216 V at 80 °C, increases from 54.9% at 30 °C to 60.6% at 80 °C.

Zeng et al.[43] attributed the lowering of cell voltage at high temperature to the decrease of polarizations at the anode and cathode. However, the potential drop in the electrolyte was not taken into account. At a high current density, the overpotential due to ionic resistance shares a large part of the overpotential for water electrolysis. In order to distinguish the overpotential due to ionic resistance from other factors, the ionic resistance is investigated with a model of the diaphragm−electrolyte system. It assumes that 30 wt % KOH solution infiltrates homogeneously into the diaphragm, and there is no gas bubbles blocking the openings of the diaphragm. The ionic resistivity of the diaphragm−electrolyte system, ρ_{D+E}, depends on the intrinsic properties of the diaphragm and the ionic resistivity of KOH solutions, ρ_E, so that it can be expressed as[44,45]

$$\rho_{D+E} = \rho_E \cdot \frac{\tau^2}{\varepsilon\omega} \tag{10}$$

where τ is the tortuosity which is defined as the ratio of actual pore lengths and diaphragm thickness, ε is the porosity, and ω is the wettability factor. The ionic resistivity of a KOH solution, ρ_E, is related to the specific conductivity, κ_E, by

$$\rho_E = \frac{1}{\kappa_E} \tag{11}$$

where κ_E is temperature-dependent, and it can be calculated by an empirical equation in reference 46. The molarity of 30 wt % KOH, which is 6.851 mol·l^{-1}, is used for calculations, resulting to the resistivities of electrolyte at temperatures from 30 to 80 °C. In this study, only Zirfon diaphragms are used, so that $\frac{\tau^2}{\varepsilon\omega}$, which is determined by the intrinsic properties of diaphragms, is assumed to be constant. The typical ionic resistivities of 0.5 mm thick Zirfon diaphragms in 32 wt % KOH solution are reported to be 4 Ω·cm at 30 °C and 2 Ω·cm at 80 °C.[29] The ionic resistivities of 32 wt % KOH solution are 1.393 Ω·cm at 30 °C and 0.675 Ω·cm at 80 °C. The value of $\frac{\tau^2}{\varepsilon\omega}$ can be derived, which is 2.917 ± 0.045. Equation 10 can be simplified to

$$\rho_{D+E} = 2.917\rho_E \tag{12}$$

The overpotential due to ionic resistance in the diaphragm−electrolyte system can be expressed as

$$\Delta U = I \cdot R_{D+E} = I \cdot \rho_{D+E} \cdot \frac{L}{A} = 2.917 I \cdot \rho_E \cdot \frac{L}{A} \tag{13}$$

where L represents the thickness of the Zirfon diaphragm (0.5 mm), and A is the effective geometric area of the diaphragm, which equals the cell area of 19.63 cm^2. A current density of 502 mA·cm^{-2} is used for calculation. The calculated overpotentials, which are shown in Figure 6b, decrease from 0.486 V at 30 °C down to 0.211 V at 80 °C with a difference of 0.275 V. The difference exactly equals the decrease of the cell voltage from 30 to 80 °C, indicating the change of cell voltage with temperature mainly attributed to the change in ionic conductivity of the electrolyte.

The cell voltage, compensated with the potential drop in electrolyte, does not have apparent temperature dependence (violet circles in Figure 6a). From 30 to 80 °C, all values are distributed in the range of 1.794 to 1.815 V. The difference between the compensated voltage and the corresponding equilibrium voltage is plotted in Figure 6c. The voltage difference represents the overpotential due to all factors except ionic resistance, containing activation overpotentials for the HER and OER, the overpotentials due to electrical resistance and gas bubble blockage, as well as other unanalyzed factors. From 30 to 50 °C, the voltage difference increases from 0.542 to 0.577 V. The reason is still unclear, requiring further study. From 50 to 80 °C, the voltage difference is almost constant with an average value of 0.579 V, which, on the other hand, confirms the change of cell voltage caused by the change of potential drop in electrolyte.

Pressure-Dependent Gas Bubble Blockage. Gas bubbles on the electrodes and the openings of the diaphragm add overpotentials for water electrolysis. The influence of pressure on the overpotential caused by gas bubble blockage was studied at the current density of 502 mA·cm^{-2}. Figure 7 shows the cell voltages measured during pressurization processes at temperatures of 30, 60, and 80 °C. At 30 °C, the cell voltage is 2.400 V at 1 bar. With the increase of pressure from 1 to 15 bar, the cell voltage decreases monotonically by 0.116 V. At pressures higher than 15 bar, the cell voltages fluctuates in the range of 2.279 ± 0.005 V. The decrease of cell

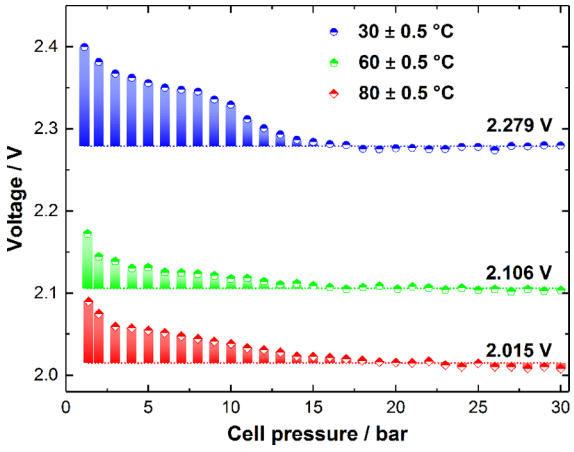

Figure 7. Pressure-dependent cell voltages measured at the current density of 502 mA·cm^{-2}.

DOI: 10.1021/acssuschemeng.7b04173
ACS Sustainable Chem. Eng. 2018, 6, 4829−4837

voltage along with the increase of pressure is also observed at 60 and 80 °C. From 1 to 30 bar, the cell voltages decreases by 0.067 V at 60 °C and 0.074 V at 80 °C. Moreover, most of the voltage reduction occurs at pressures lower than 15 bar. At pressures higher than 15 bar, the cell voltages fluctuates around 2.106 V at 60 °C and 2.015 V at 80 °C. The fluctuation of voltages can be attributed to the temperature fluctuation during the measurements.

Appleby et al.[47] reported pressure-dependent cell voltages in an alkaline water electrolyzer operating at 80 °C, and the majority of the voltage decrease occurred at pressures less than 10 atm. Zeng et al.[43] summarized the gas bubble phenomenon in alkaline water electrolyzers, and also mentioned that elevated cell pressure (up to 35 bar) is able to reduce the bubble sizes and to minimize the resistances from gas bubble blockage. Sillen et al.[48] discussed the growth of gas bubbles on electrodes, and suggested that gas bubble nucleation occurs at activated cavities on the electrode surface. The mouth radius of activated cavities, R_0, is pressure-dependent, which can be expressed as[48]

$$R_0 = \frac{2\sigma}{\Delta C_0} \cdot \frac{C_s}{P} \tag{14}$$

where σ represents the surface tension, P represents the pressure, ΔC_0 and C_s are the supersaturation value and saturation concentration, respectively. For fixed electrodes and electrolyte, all parameters except pressure are constant at a certain temperature. The increase of cell pressure can activate small cavities for gas bubble nucleation. The growth of gas bubbles is controlled by the mass diffusion of hydrogen molecules. When bubbles are big enough, they reach the critical state for detachment. Jones et al.[49] pointed out that the bubble radius at detachment is proportional to the cubic root of the cavity mouth radius. Therefore, at high pressure, small cavities are activated for bubble nucleation, and bubbles nucleated at small cavities detach from the electrode surface at relatively small sizes. The frequent nucleation and detachment of small gas bubbles are more efficient for transporting gases from the electrode−electrolyte interface, so that the overpotential caused by gas bubble blockage can be reduced. The advantage of pressurization to the cell voltage can be observed only at pressures lower than a critical value. In this work, the critical value is around 15 bar. Further increase of cell pressure does not reduce the cell voltage anymore. The critical pressure may be different, when different electrode or electrolyte is used, or gases are produced at different rates. The critical pressure characterized with this system may suggest an upper limit of operating pressure to improve the voltage efficiency without significantly sacrificing hydrogen purity.

CONCLUSIONS

A lab-scale system for alkaline water electrolysis has been developed. This system can significantly advance the lab-scale material research and bridge the intrinsic properties of materials with their performance under realistic operating conditions. It is able to work up to 30 bar and 80 °C with continuous liquid circulation. The system has been demonstrated by running experiments with nickel plates and Zirfon diaphragms. Increasing the operating temperature and pressure can significantly improve the voltage efficiency, which could be verified in this work. The overall cell voltage at high current density strongly depends on the cell temperature, but, if temperature-dependent ionic conductivity is taken into account, the remaining overpotential contributed by electrode activation, electrical resistance and gas bubble blockage is almost constant. The elevated cell pressure can reduce the bubble sizes, and, as a result, the resistance from gas-bubble blockage can be minimized. However, the advantage may disappear when pressure is higher than a critical value. The purpose of further increasing system pressure is to reduce the energy consumption required for gas compression in subsequent steps. AW electrolyzers based on state-of-the-art materials are still not suitable for operating with intermittent power supply. Working at a low current density or at a standby mode leads to low gas purities and even safety issues. For better tolerance to intermittent power supply, further developments of materials and system design are still required.

AUTHOR INFORMATION

Corresponding Author

*U. Vogt. Email: Ulrich.Vogt@empa.ch.

ORCID

Ulrich F. Vogt: 0000-0002-7974-9799

Notes

The authors declare no competing financial interest.

ACKNOWLEDGMENTS

We acknowledge financial support from the European Union's Seventh Framework Programme (FP7/2007-2013) for the Fuel Cells and Hydrogen Joint Technology Initiative under grant agreement no. 278824. The research was also funded by Swiss Federal Office of Energy through the P&D project PALE under grant agreement no. 8100146-02 and by Swisselectric Research in the project alkaline electrolysis for renewable energy generation.

REFERENCES

(1) Global energy statistical yearbook 2017. Enerdata intelligence and consulting: https://yearbook.enerdata.net/, 2017.

(2) Turner, J. A. Sustainable hydrogen production. *Science* **2004**, *305*, 972−974.

(3) Veziroglu, A.; Macario, R. Fuel cell vehicles: State of the art with economic and environmental concerns. *Int. J. Hydrogen Energy* **2011**, *36* (1), 25−43.

(4) Eberle, U.; Muller, B.; von Helmolt, R. Fuel cell electric vehicles and hydrogen infrastructure: status 2012. *Energy Environ. Sci.* **2012**, *5* (10), 8780−8798.

(5) Pellow, M. A.; Emmott, C. J. M.; Barnhart, C. J.; Benson, S. M. Hydrogen or batteries for grid storage? A net energy analysis. *Energy Environ. Sci.* **2015**, *8* (7), 1938−1952.

(6) Gutiérrez-Martín, F.; Guerrero-Hernández, I. Balancing the grid loads by large scale integration of hydrogen technologies: The case of the Spanish power system. *Int. J. Hydrogen Energy* **2012**, *37* (2), 1151−1161.

(7) Beaudin, M.; Zareipour, H.; Schellenberglabe, A.; Rosehart, W. Energy storage for mitigating the variability of renewable electricity sources: An updated review. *Energy Sustainable Dev.* **2010**, *14* (4), 302−314.

(8) Lide, D. R.; Baysinger, G.; Berger, L. I.; Goldberg, R. N.; Kehiaian, H. V.; Kuchitsu, K.; Rosenblatt, G.; Roth, D. L.; Zwillinger, D. *CRC Handbook of Chemistry and Physics, Internet Version 2005*; CRC Press: Boca Raton, FL, USA, 2005.

(9) Carmo, M.; Fritz, D. L.; Mergel, J.; Stolten, D. A comprehensive review on PEM water electrolysis. *Int. J. Hydrogen Energy* **2013**, *38* (12), 4901−4934.

(10) Grigoriev, S. A.; Porembsky, V. I.; Fateev, V. N. Pure hydrogen production by PEM electrolysis for hydrogen energy. *Int. J. Hydrogen Energy* **2006**, *31* (2), 171−175.

DOI: 10.1021/acssuschemeng.7b04173
ACS Sustainable Chem. Eng. 2018, 6, 4829−4837

(11) Phillips, R.; Dunnill; Charles, W. Zero gap alkaline electrolysis cell design for renewable energy storage as hydrogen gas. *RSC Adv.* **2016**, *6* (102), 100643−100651.
(12) Santos, D. M. F.; Sequeira, C. A. C.; Figueiredo, J. L. Hydrogen production by alkaline water electrolysis. *Quim. Nova* **2013**, *36* (8), 1176−1193.
(13) Pavel, C. C.; Cecconi, F.; Emiliani, C.; Santiccioli, S.; Scaffidi, A.; Catanorchi, S.; Comotti, M. Highly efficient platinum group metal free based membrane-electrode assembly for anion exchange membrane water electrolysis. *Angew. Chem., Int. Ed.* **2014**, *53* (5), 1378−1381.
(14) Leng, Y.; Chen, G.; Mendoza, A. J.; Tighe, T. B.; Hickner, M. A.; Wang, C. Y. Solid-state water electrolysis with an alkaline membrane. *J. Am. Chem. Soc.* **2012**, *134* (22), 9054−9057.
(15) Koponen, J.; Kosonen, A.; Ruuskanen, V.; Huoman, K.; Niemelä, M.; Ahola, J. Control and energy efficiency of PEM water electrolyzers in renewable energy systems. *Int. J. Hydrogen Energy* **2017**, *42* (50), 29648−29660.
(16) Danilovic, N.; Ayers, K. E.; Capuano, C.; Renner, J. N.; Wiles, L.; Pertoso, M. (Plenary) Challenges in Going from Laboratory to Megawatt Scale PEM Electrolysis. *ECS Trans.* **2016**, *75* (14), 395−402.
(17) Varcoe, J. R.; Atanassov, P.; Dekel, D. R.; Herring, A. M.; Hickner, M. A.; Kohl, P. A.; Kucernak, A. R.; Mustain, W. E.; Nijmeijer, K.; Scott, K.; Xu, T.; Zhuang, L. Anion-exchange membranes in electrochemical energy systems. *Energy Environ. Sci.* **2014**, *7* (10), 3135−3191.
(18) Vincent, I.; Bessarabov, D. Low cost hydrogen production by anion exchange membrane electrolysis: A review. *Renewable Sustainable Energy Rev.* **2018**, *81* (2), 1690−1704.
(19) Ursua, A.; Gandia, L. M.; Sanchis, P. Hydrogen production from water electrolysis: Current status and future trends. *Proc. IEEE* **2012**, *100* (2), 410−426.
(20) Mergel, J.; Carmo, M.; Fritz, D. Status on Technologies for Hydrogen Production by Water Electrolysis. In *Transition to Renewable Energy Systems*; Stolten, D., Scherer, V., Eds.; Wiley-VCH GmbH & Co. KGaA: Weinheim, Germany, 2013.
(21) Wendt, H.; Imarisio, G. Nine years of research and development on advanced water electrolysis. A review of the research programme of the Commission of the European Communities. *J. Appl. Electrochem.* **1988**, *18*, 1−14.
(22) Janssen, H.; Bringmann, J. C.; Emonts, B.; Schroeder, V. Safety-related studies on hydrogen production in high-pressure electrolysers. *Int. J. Hydrogen Energy* **2004**, *29* (7), 759−770.
(23) LeRoy, R. L. Industrial water electrolysis: present and future. *Int. J. Hydrogen Energy* **1983**, *8* (6), 401−417.
(24) *CONTHOS 2 Thermal Conductivity Gas Analyzer Operator's Manual*; LFE GmbH & Co KG: Maintal, Germany, 2004.
(25) *High performance series Micro annular gear pump mzr®-7205 For industrial production and process technology*; HNP Mikrosysteme GmbH: Schwerin, Germany, 2015.
(26) *TSX Series Programmable High Current DC Power Supply Instruction Manual*; AIM-TTI Ltd.: Combridgeshire, UK, 2009.
(27) Gorlin, M.; Ferreira de Araujo, J.; Schmies, H.; Bernsmeier, D.; Dresp, S.; Gliech, M.; Jusys, Z.; Chernev, P.; Kraehnert, R.; Dau, H.; Strasser, P. Tracking Catalyst Redox States and Reaction Dynamics in Ni-Fe Oxyhydroxide Oxygen Evolution Reaction Electrocatalysts: The Role of Catalyst Support and Electrolyte pH. *J. Am. Chem. Soc.* **2017**, *139* (5), 2070−2082.
(28) Vermeiren, P.; Adriansens, W.; Moreels, J. P.; Leysen, R. Evalucation of the Zirfon® separator for use in alkaline water electrolysis and Ni-H2 batteries. *Int. J. Hydrogen Energy* **1998**, *23*, 321−324.
(29) Vermeiren, P.; Adriansens, W.; Moreels, J. P.; Leysen, R. The Composite Zirfon® Separator for Alkaline Water Electrolysis. In *Hydrogen Power: Theoretical and Engineering Solutions: Proceedings of the Hypothesis II Symposium*, Grimstad, Norway, 18−22 August 1997; Saetre, T. O., Ed.; Springer Netherlands: Dordrecht, 1998; pp 179−184.
(30) Shoor, S. K.; Walker, R. D., Jr.; Gubbins, K. E. Salting out of nonpolar gases in aqueous potassium hydroxide solutions. *J. Phys. Chem.* **1969**, *73* (2), 312−317.
(31) Tham, M. K.; Walker, R. D., Jr.; Gubbins, K. E. Diffusion of oxygen and hydrogen in aqueous potassium hydroxide solutions. *J. Phys. Chem.* **1970**, *74* (8), 1747−1751.
(32) Schalenbach, M.; Lueke, W.; Stolten, D. Hydrogen diffusivity and electrolyte permeability of the Zirfon PERL separator for alkaline water electrolysis. *J. Electrochem. Soc.* **2016**, *163* (14), F1480−F1488.
(33) Soares, D. M.; Teschke, O.; Torriani, I. Hydride Effect on the Kinetics of the Hydrogen Evolution Reaction on Nickel Cathodes in Alkaline Media. *J. Electrochem. Soc.* **1992**, *139* (1), 98−105.
(34) Conway, B. E.; Angerstein-Kozlowska, H.; Sattar, M. A.; Tilak, B. V. Study of a Decomposing Hydride Phase at Nickel Cathodes by Measurement of Open-Circuit Potential Decay. *J. Electrochem. Soc.* **1983**, *130* (9), 1825−1836.
(35) Machado, S. A. S.; Avaca, L. A. The hydrogen evolution reaction on nickel surfaces stabilized by H-adsorption. *Electrochim. Acta* **1994**, *39* (10), 1385−1391.
(36) Lyons, M. E. G.; Brandon, M. P. A comparative study of the oxygen evolution reaction on oxidised nickel, cobalt and iron electrodes in base. *J. Electroanal. Chem.* **2010**, *641* (1), 119−130.
(37) Rossmeisl, J.; Logadottir, A.; Nørskov, J. K. Electrolysis of water on (oxidized) metal surfaces. *Chem. Phys.* **2005**, *319* (1−3), 178−184.
(38) Kibria, M. F.; Mridha, M. S. Electrochemical studies of the nickel electrode for the oxygen evolution reaction. *Int. J. Hydrogen Energy* **1996**, *21* (3), 179−182.
(39) Choquette, Y.; Ménard, H.; Brossard, L. Electrocatalytic performance of composite-coated electrodes for alkaline water electrolysis. *Int. J. Hydrogen Energy* **1990**, *15* (1), 21−26.
(40) Nadesan, J. C. B.; Tseung, A. C. C. Oxygen Evolution on Nickel Oxide Electrodes. *J. Electrochem. Soc.* **1985**, *132* (12), 2957−2959.
(41) Miles, M. H.; Kissel, G.; Lu, P. W. T.; Srinivasan, S. Effect of Temperature on Electrode Kinetic Parameters for Hydrogen and Oxygen Evolution Reactions on Nickel Electrodes in Alkaline Solutions. *J. Electrochem. Soc.* **1976**, *123* (3), 332−336.
(42) Roy, A.; Watson, S.; Infield, D. Comparison of electrical energy efficiency of atmospheric and high-pressure electrolysers. *Int. J. Hydrogen Energy* **2006**, *31* (14), 1964−1979.
(43) Zeng, K.; Zhang, D. Recent progress in alkaline water electrolysis for hydrogen production and applications. *Prog. Energy Combust. Sci.* **2010**, *36* (3), 307−326.
(44) Vermeiren, P.; Leysen, R.; Beckers, H.; Moreels, J. P.; Claes, A. The influence of manufacturing parameters on the properties of macroporous Zirfon® separators. *J. Porous Mater.* **2008**, *15* (3), 259−264.
(45) Stojadinovic, J.; Wiedenmann, D.; Gorbar, M.; Mantia, F. L.; Suarez, L.; Zakaznova-Herzog, V.; Vogt, U. F.; Grobety, B.; Zuttel, A. Electrochemical Characterization of Porous Diaphragms in Development for Gas Separation. *ECS Electrochem. Lett.* **2012**, *1* (4), F25−F28.
(46) Gilliam, R. J.; Graydon, J. W.; Kirk, D. W.; Thorpe, S. J. A review of specific conductivities of potassium hydroxide solutions for various concentrations and temperatures. *Int. J. Hydrogen Energy* **2007**, *32* (3), 359−364.
(47) Appleby, A. J.; Crepy, G.; Jacquelin, J. High efficiency water electrolysis in alkaline solution. *Int. J. Hydrogen Energy* **1978**, *3* (1), 21−37.
(48) Sillen, C. W. M. P.; Barendrecht, E.; Janssen, L. J. J.; van Stralen, S. J. D. Gas bubble behaviour during water electrolysis. *Int. J. Hydrogen Energy* **1982**, *7* (7), 577−587.
(49) Jones, S. F.; Evans, G. M.; Galvin, K. P. Bubble nucleation from gas cavities - a review. *Adv. Colloid Interface Sci.* **1999**, *80*, 27−50.

DOI: 10.1021/acssuschemeng.7b04173
ACS Sustainable Chem. Eng. 2018, 6, 4829−4837